*Journal of Power Sources*, 3 (1978) 67 - 80



# ELECTROLYTES FOR THE HIGH TEMPERATURE FUEL CELL; EXPERIMENTAL AND THEORETICAL STUDIES OF THE PEROVSKITE $LaAlO_3$*

J. A. KILNER, P. BARROW and R. J. BROOK

*Department of Ceramics, University of Leeds, Leeds LS2 9JT (Gt. Britain)*

M. J. NORGETT

*Theoretical Physics Division, A.E.R.E., Harwell, Oxon OX11 0RA (Gt. Britain)*

(Received November 5, 1977)

## Summary

We present electrical conductivity measurements on a range of samples, based on the perovskite oxide $LaAlO_3$, in the temperature span 600 - 1000 °C and under controlled partial pressures of oxygen The conductivity is described for a series of compositions made oxygen deficient by replacement of either the $La^{3+}$ or $Al^{3+}$ cations by the divalent cations $Ca^{2+}$, $Mg^{2+}$, $Sr^{2+}$. We also present transport number measurements which indicate that charge transport in these materials is purely ionic for reducing atmospheres ($pO_2 \sim 10^{-14}$ atm.). The Arrhenius energies calculated from the ionic conductivities fall in the range 1.0 to 3 eV.

We have made calculations, using the general purpose computer programme HADES, for the enthalpies of defect formation, migration, and for the energies of association between dopant and defect. These are compared with the experimentally determined values. Finally, details of the microstructure of the materials are given and these are discussed in view of the experimental results.

## Introduction

Our programme is aimed at developing a basis for the prediction of fast ion transport in solids by using calculations based on interatomic potentials. We are currently in the initial stages of this programme which involves the calculation and measurement of defect formation and migration energies for

*Paper presented at The International Symposium on Molten Electrolytes and High Temperature Batteries organized by the Electrochemistry Group of the Chemical Society, Brighton, Gt. Britain, September 22 - 23, 1977.

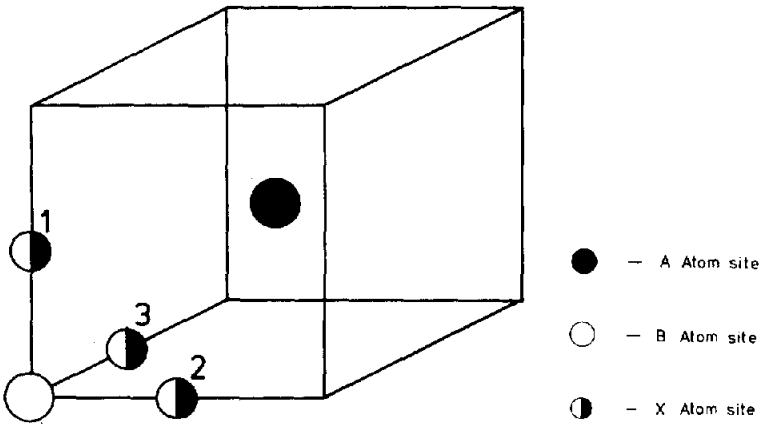


Fig. 1. The unit cell for the cubic perovskite $ABX_3$ showing the individual atom sites.

a known ion conductor, $LaAlO_3$, which has been shown to exhibit substantial anion conduction [1, 2].

*Perovskite structure*

The perovskite structure is shown in Fig. 1 for an imaginary compound $ABX_3$. In $LaAlO_3$ the $La^{3+}$ ion occupies the A site at the body centre of the cube, the $Al^{3+}$ ion occupies the cube corner B site and the $O^{2-}$ ions occupy the X sites along the cube edges. The cubic structure shown is the idealized perovskite structure; most perovskites are either rhombohedral or tetragonal distortions of this idealized structure. $LaAlO_3$ is rhombohedral at room temperature and transforms to the cubic structure at a temperature of ~ 700 K [3].

We have prepared several oxygen deficient materials based on $LaAlO_3$ by doping both cation sites with divalent cations. The nomenclature we have adopted to represent these materials is as follows. For example, for calcium doped materials:

$X\%$ $Ca_{Al}$ represents the formula

$$La(Ca_{X/100}, Al_{1-(X/100)})\, O_{3-(X/200)}$$

$X\%$ $Ca_{La}$ represents the formula

$$(Ca_{X/100}, La_{1-(X/100)})\, Al\, O_{3-(X/200)}$$

This nomenclature will be used exclusively in this paper.

*Preparation of materials*

The samples were prepared from intimately mixed powders consisting of the correct proportion of the relevant oxides. These mixed oxides were

produced by two methods: (1) hot paraffin drying of a solution of the respective nitrates, (2) co-precipitation of the respective oxalates.

To produce oxides from these mixtures the powders were calcined in air at 1000 K, and then milled to produce a fine powder. These fine mixed oxide powders were then heated to a temperature of between 1273 and 1573 K in air until they gave an X-ray diffraction pattern corresponding to the single phase perovskite. Usually this took around 24 hours but the exact period of time depends upon the particular composition being prepared and the starting route, the hot paraffin produced powder being the more reactive. Sintered specimens were obtained by milling the powders, pressing to shape, and finally firing at a temperature of 1873 K for 12 hours in pure oxygen. By using this method samples of density up to 95% theoretical density could be obtained, although it is realized that there are difficulties in achieving exact stoichiometry.

Two types of sintered sample were made: a disc of diameter 1.9 cm by ~ 3 mm thick, and a cylinder of diameter 1.3 cm by ~ 1.5 cm long. Porous platinum electrodes were fabricated by sintering platinum paste onto the surface of the specimens.

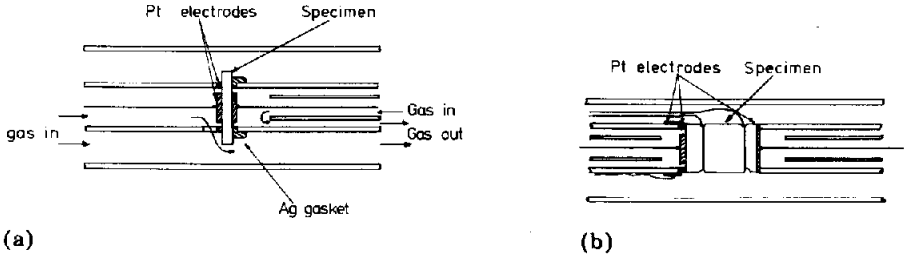


**Fig. 2. The apparatus used for the electrical measurements showing (a) the transport number cell, and (b) the conductivity rig.**

*Apparatus*

The disc specimens were used for measurement of the transport number using the apparatus shown in Fig. 2(a). The specimen is supported by alumina tubes which form two chambers into which two gas streams can be introduced, thus forming an electrochemical cell. The gas in the outer chamber, surrounding the specimen, is the same as that in the l.h. chamber. A silver gasket prevents any mixing of the gases in the outer and r.h. chamber. The e.m.f. generated by the cell is sensed by two platinum wires down the centre of the cell which are connected to an external measurement circuit.

Two types of gas mixture were used to cover the range of $pO_2$ values. For oxidizing conditions oxygen was run against oxygen/argon mixtures: for reducing conditions two different $CO/CO_2$ gas mixtures were used.

The conductivity measurements were made by a guarded four point technique, using the cylindrical samples, in the apparatus shown in Fig. 2(b). These samples had electrodes on the front and rear faces to which a potential was applied. These electrodes included a guard ring. The voltage probes consisted of Pt wires set into grooves around the sample surface, equidistant from the front and rear surfaces. The apparatus was totally enclosed in a silica envelope and could be filled with the same atmospheres as the transport number cell.

The electrical circuit used for the resistance measurements is shown in Fig. 3. This is a conventional 4 point arrangement except that the guard and

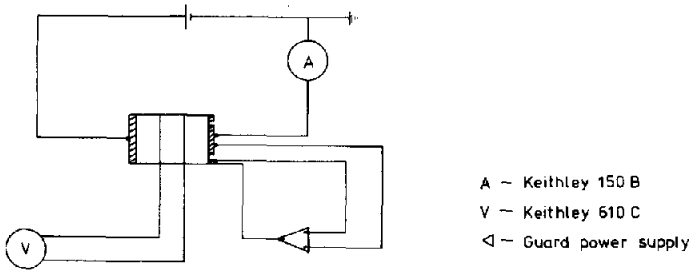


Fig. 3. The electrical circuit used for the conductivity measurements.

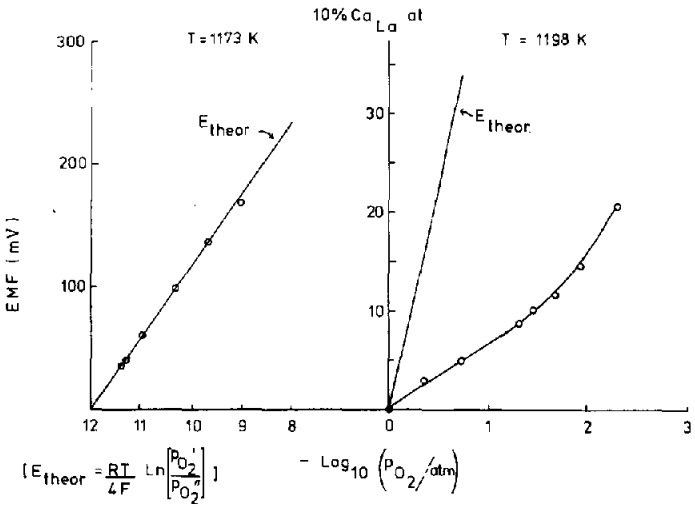


Fig. 4. The results from the transport number cell using a 10% $Ca_{La}$ sample. The e.m.f. generated across the cell is plotted as a function of oxygen partial pressure. The right hand curve corresponds to oxidizing conditions using oxygen as a standard gas; the left hand curve corresponds to reducing conditions, the standard gas here giving an oxygen partial pressure of $10^{-12}$ atm.

inner electrodes are kept at the same potential by an operational amplifier. This guards against any errors due to surface or gas phase conduction at high temperatures.

*Results*

In Fig. 4 the results of experiments using the transport number cell on a 10% $Ca_{La}$ sample are shown. The e.m.f. generated across the cell is plotted against the variation of oxygen partial pressure in the r.h. chamber. The right hand curve at $T$ = 1198 K corresponds to the oxidizing conditions with oxygen as a standard gas in the r.h. chamber. The line marked $E_{theor}$ is given by the equation:

$$E_{theor} = \frac{RT}{4F} \ln \frac{P_{O_2'}}{P_{O_2''}} \tag{1}$$

where $P_{O_2'}$ and $P_{O_2''}$ refer to the oxygen partial pressures at each side of the cell; $R$ is the gas constant; $F$ is the Faraday; $T$ is the absolute temperature. The measured points, for the oxidizing conditions, fall well below the theoretical line indicating that transport is only partially ionic at these partial pressures. The l.h. curve corresponds to reducing conditions; the standard gas used here gave an oxygen partial pressure of $10^{-12}$ atm. at 1173 K. Here it would seem that transport is purely ionic, as the observed points agree well with the $E_{theor}$ line.

These data can be translated into transport number data as shown in Fig. 5. The number plotted here is the average transport number over the range of partial pressure in the electrochemical cell, and is defined by:

$$\tilde{t}_i = \frac{E_{meas}}{E_{theor}} \tag{2}$$

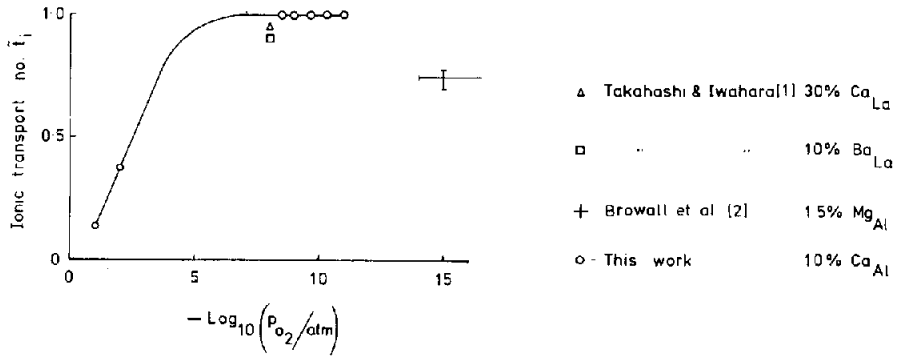


Fig. 5. The average ionic transport number $\tilde{t}_i$ plotted as a function of oxygen partial pressure for $LaAlO_3$ based materials.

Included in Fig. 5 are data taken from Takahashi [1] and Browall [2] for comparison. Our data are in good agreement with those of Takahashi and Iwahara, especially when it is noted that their results are averaged over $P_{O_2}$ values from air to reducing atmospheres ($\sim 10^{-8}$ atm.). The data of Browall *et al.* may indicate that $\tilde{t}_i$ is dropping in the range $P_{O_2} \sim 10^{-15}$ atm.; however, this result could be brought about by a low density sample through which gas can diffuse, especially as they report no density for their samples.

The low value of $t_i$ at the oxidizing atmospheres is probably due to conduction by electron holes. These can be created by the following reaction, given in Kröger–Vink notation:

$$V\ddot{o} + \tfrac{1}{2} O_2 \rightleftharpoons O_O^x + 2h^{\cdot} \qquad (3)$$

This equation implies that the hole contribution will vary as $P_{O_2}^{1/4}$, under conditions where overall neutrality is principally achieved by, *e.g.* $[Ca'_{La}] = 2[V\ddot{o}]$. For the doped material we can thus predict the shape of the log ($\sigma$) *vs.* log ($P_{O_2}$) plot as we proceed from oxidizing to reducing atmospheres. At very low oxygen partial pressures where $t_i$ is 1, the conductivity will remain constant, fixed by the dopant level which determines the oxygen vacancy concentration. At high values of $P_{O_2}$ the hole conduction will become important, and the slope of the log ($\sigma$) *vs.* log ($P_{O_2}$) will change to $\frac{1}{4}$.

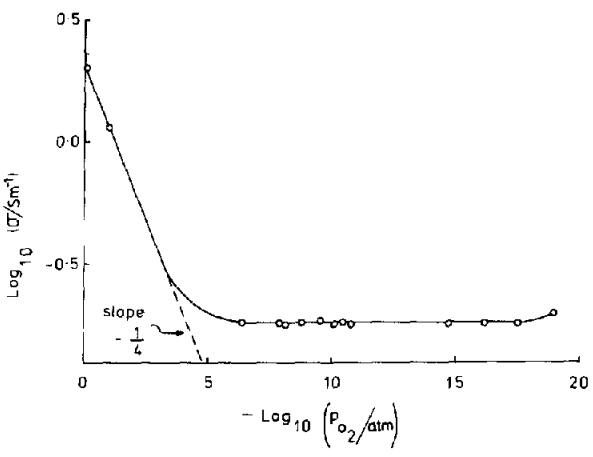


Fig. 6. The variation of $\log_{10}(\sigma)$ as a function of $-\log_{10}(P_{O_2})$ for a 10% $Ca_{Al}$ sample at $t$ = 1198 K. Also shown is the slope predicted from consideration of the electron hole component arising at high values of $P_{O_2}$.

Figure 6 shows the log ($\sigma$) *vs.* $-\log (P_{O_2})$ plot for a 10% $Ca_{Al}$ sample at 1198 K, and as predicted from the above arguments, the shape of the curve is consistent with hole conduction predominating at high partial pressures of oxygen. The flat part of the curve where $t_i$ is 1, extends the transport number measurements and infers that the range of oxygen partial pressures for which $t_i$ is 1 extends from $\sim 10^{-6}$ to $10^{-18}$ atm. The conductivity measure-

ments presented in the following sections were all performed under oxygen partial pressures between $10^{-12}$ to $10^{-14}$ atm., well in the centre of the ionic range.

The Arrhenius plots obtained from the conductivity measurements are shown in Fig. 7; also included in Fig. 7 are data taken from Browall *et al.* [2] for a 15% $Mg_{Al}$ sample. All the plots are straight lines with no change in slope. Values of $(\sigma T)_0$ and the Arrhenius energy $E_A$ fitted to these plots are given in Table 1. The values for the lightly doped samples, *i.e.* those with 2.5% and 5% dopant level, all fall close together with the exception of the 2.5% $Sr_{La}$ sample. All the measured Arrhenius energies fall between 1.0 and 3.0 eV, the lowest observed value being 1.0 eV.

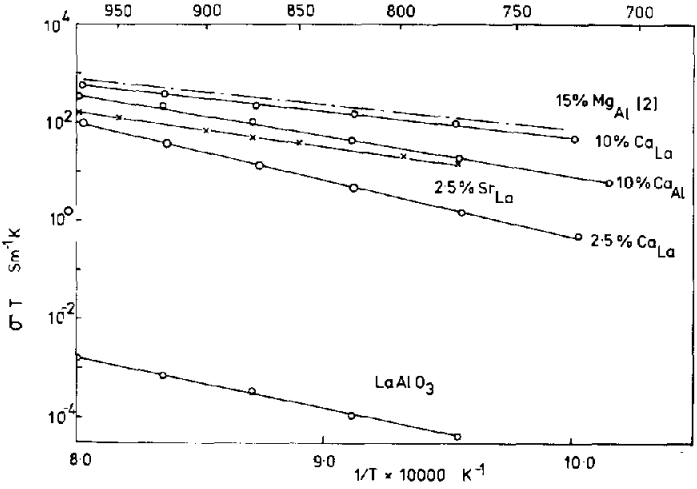


Fig. 7. Arrhenius plots of the conductivity for a range of samples based on $LaAlO_3$. These plots were obtained under a controlled atmosphere of oxygen giving an oxygen partial pressure of $P_{O_2} \sim 10^{-12} - 10^{-14}$ atm.

TABLE 1

Conductivity data

| Sample | $Log_{10}(\sigma T)_0$ | $E_A$ (eV) |
|---|---|---|
| 10% $Ca_{La}$ | 6.8 | 1.0 |
| 5% $Ca_{La}$ | 11.0 | 2.3 |
| 2.5% $Ca_{La}$ | 11.0 | 2.2 |
| 5% $Ca_{Al}$ | 10.8 | 2.2 |
| 10% $Ca_{Al}$ | 9.2 | 1.6 |
| 2.5% $Mg_{Al}$ | 9.8 | 2.0 |
| 2.5% $Sr_{La}$ | 8.0 | 1.3 |
| Pure | — | 1.9 |

## The calculations

The calculation of defect formation and vacancy migration energies used the computer programme HADES, which calculates the energy of a defect on the basis of interatomic potentials. Briefly, the lattice is represented by an assembly of polarizable ions interacting by some specific potential which includes contributions from Coulomb, polarization and short-range repulsive interactions. The calculation method involves finding the relaxations of the defect lattice which give a minimum lattice potential energy. For all our calculations we are dealing with charged defects and thus in order to calculate these lattice relaxations the lattice is split into two regions: in an inner region, the lattice relaxations are calculated explicitly and are matched to a boundary region where the lattice distortion is calculated assuming the material responds as a harmonic dielectric continuum to the electric field of the defect.

Using this calculation scheme the defect formation energies are calculated as the difference between the lattice potential energies of the perfect and defect lattices. Migration activation energies for defects correspond to the differences in energy between the equilibrium and lowest saddle point between two such configurations. Further details of the exact methods of calculation used in the HADES programme are given in Lidiard and Norgett [4] and Norgett [5].

*Interatomic potentials*

The interatomic potentials used for defect calculations must be able to reproduce accurately both the dielectric and elastic properties of the lattice. The simplest ionic model which is satisfactory in this respect is the shell model. In this model the ions are represented by a separate charged core coupled to a charged shell by isotropic harmonic forces. The short range interatomic forces are then assumed to act through the shells of the ions. This type of model has been used extensively in the field of lattice dynamics and has recently been applied to the field of defect calculations.

The cation–anion interatomic potentials are readily expressed by the exponential form:

$$V_{+-} = A_{+-} \exp(-r/\rho_{+-}) \tag{4}$$

Anion–anion interactions are better represented by the Buckingham potential:

$$V_{--} = A_{--} \exp(-r/\rho_{--}) - C_{--}/r^6 \tag{5}$$

in which the repulsive interaction is supplemented by an attractive van der Waals term.

The values of $A$, $\rho$ and $C$ are arrived at empirically by using a separate programme which fits the potential parameters to the measured lattice parameter, cohesive energy, dielectric constants, etc. This type of analysis and defect calculation has been used successfully to obtain defect energies in

several systems including the oxides MgO [6], $UO_2$ [7] and FeO, CoO and NiO [8].

For $LaAlO_3$ very little of this necessary physical data are known and so, in order to obtain potentials for the defect calculations, several approximations are therefore required. We have neglected all anion–anion interactions on the basis of the experience gained with the other oxides. There is little error in neglecting these terms as Coulomb interactions tend to prevent the close approach of anions, so that $V_{--}$ contributes little to the total energy. We have also taken the parameters for the $Al^{3+}$–$O^{2-}$ interaction to be the same as those of the $Mg^{2+}$–$O^{2-}$ interaction; this is reasonable as the $Mg^{2+}$ and $Al^{3+}$ ions are isoelectronic.

Shell model parameters are usually chosen to fit to the values of dielectric constants, but again, for $LaAlO_3$, these are not available and we have therefore assumed that only the oxygen ion is polarizable and that the shell charge is the same as that found in MgO.

The parameters for the $La^{3+}$–$O^{2-}$ interaction were then found by fitting the interatomic separation for the minimum in the lattice potential energy to the known lattice parameter; however, with two adjustable parameters fitted to only one known value these fitted values are not unique. The final set of parameters chosen for the $La^{3+}$–$O^{2-}$ interaction were those which gave the lowest positive static dielectric constant for the $LaAlO_3$ structure, and these are given in Table 2.

TABLE 2

Potential data for $LaAlO_3$

| Interaction | A (eV) | $\rho$ (Å) |
|---|---|---|
| La—O | 3172.5 | 0.3286 |
| Al—O | 1152.0 | 0.3065 |

Shell parameters $K$ in eV Å

| | | |
|---|---|---|
| $Y_O = -2.62$ | $Y_{La} = +3.0$ | $Y_{Al} = +3.0$ |
| $K_O = 38.08$ | $K_{La} = \infty$ | $K_{Al} = \infty$ |

The most important defect energies calculated for this material are given in Table 3. In the right hand column of Table 3 the energies per defect are given, as these can occur as contributions to the Arrhenius energy. From these values it is seen that the intrinsic disorder in $LaAlO_3$, as predicted by these calculations, is Schottky disorder, *i.e.* this has the lowest energy per defect. The second set of energies given in Table 3 are the vacancy migration activation energies. No value for the $Al^{3+}$ vacancy was calculated because of the extremely high defect energies associated with this cation. The two oxygen vacancy activation energies refer to the two possible migration routes for this ion; the "face" route refers to migration across the centre of the cube face of the unit cell in the ⟨100⟩ direction. The "corner" route refers to

TABLE 3

Calculated energies (eV)

| Frenkel energies | Energy/defect |
|---|---|
| $E^F_{La}$ = 29.76 | 14.88 |
| $E^F_{Al}$ = 16.51 | 8.25 |
| $E^F_O$ = 12.72 | 6.36 |
| Schottky energy | |
| $E_s$ = 16.13 | 3.23 |
| Vacancy migration activation energies | |
| $E^A_{La}$ = 6.81 | |
| $E^A_O$ = 6.95 face | |
| $E^A_O$ = 0.57 corner | |

migration across the corner of the cube face in the ⟨110⟩ direction. Clearly this "corner" jump is the most favoured mechanism of all and we can thus expect charge transport in this material to take place by oxygen vacancy migration in the absence of an electron or electron hole component. From these energies we can thus predict the Arrhenius energies expected from the conductivity data. For a doped and therefore oxygen deficient material, we should expect to see no contribution from the defect formation energy leaving only a contribution from the migration activation energy. These calculations thus suggest an Arrhenius energy of 0.57 eV for the doped material. For pure $LaAlO_3$ there will be a contribution from the formation energy as well as the migration energy and thus we expect to see an Arrhenius energy of the sum of the two: 3.23 + 0.57 = 3.80 eV.

## Discussion

In Fig. 8 the measured activation energies for $LaAlO_3$ based materials are plotted against % cation replacement, a distinction is made here between the two cation sites. The calculated value for the migration energy is marked as a dotted line on Fig. 8, and also included are the data of Browall [2] and Steele *et al.* [9]. Clearly there is a spread of values, especially for the lightly doped samples, and many of these values are higher than the calculated values; however, there appears to be a trend towards lower activation energies at higher doping levels. The value of the activation energy for our pure material is much lower than the 3.8 eV predicted from our calculations. This may be due to impurities in the pure material giving rise to extrinsic behaviour, indeed the value falls much nearer that for the lightly doped samples.

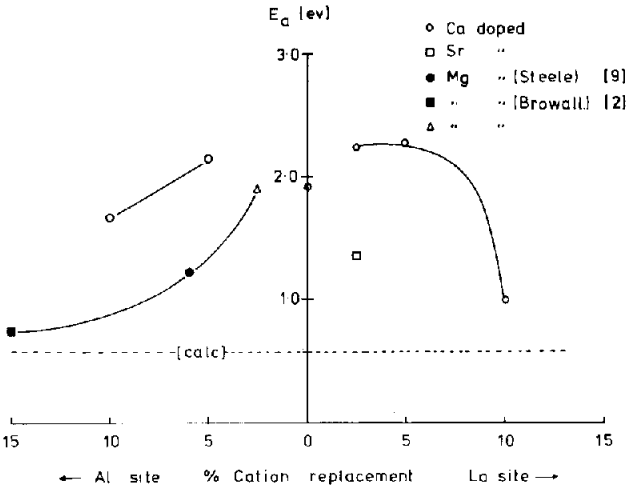


**Fig. 8. A comparison of the measured activation energies with the calculated migration energy for $LaAlO_3$ based materials.**

One possible reason for the high Arrhenius energies seen in the doped samples was thought to be the energies of association between dopant and oxygen vacancy. Calculations were made of the dissociation energy of such complexes as $(M'_{Al} - V\ddot{o} - M'_{Al})^x$ by the following reaction:

$$O_O^x + (M'_{Al} - V\ddot{o} - M'_{Al})^x \rightarrow (M'_{Al} - O_O^x - M'_{Al})'' + V\ddot{o}$$

where M represents a divalent dopant ion. The energy of dissociation of this type of defect could be as high as 1.7 eV. The contribution of this to the Arrhenius energy is only 0.85 eV giving a total energy for dissociation and migration of 0.85 + 0.57 = 1.42 eV, still slightly lower than that of the lightly doped samples.

Finally, optical and electron microscopy was performed on all the materials measured to check the microstructure and phase purity of the samples. All our samples were found to be two phase to a greater or lesser extent, even though all appeared to be single phase when examined by X-ray diffraction. An examination of several pure $LaAlO_3$ samples sintered at high temperatures indicated that this second phase can form a continuous grain boundary layer when sintered at temperatures above 1898 K. This could clearly have a marked effect upon the measured electrical properties of the samples, although our samples were prepared at a lower temperature than 1823 K; Steele [9] and Browall [2] used sintering temperatures in excess of this.

In the doped samples the second phase was found to be dispersed although quite large areas of second phase were sometimes visible. Figure 9 shows a large particle of second phase in a 2.5% Sr doped sample, taken in an S.E.M. The machine used was fitted with an energy dispersive X-ray analysis probe (EDAX) and using this, X-ray fluorescent spectra were taken of both

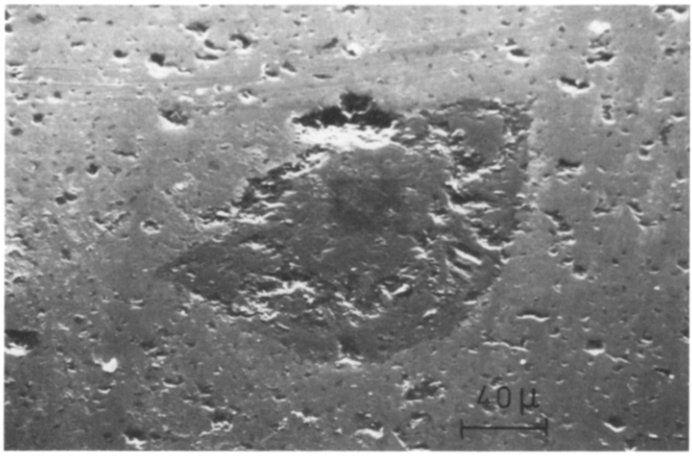


Fig. 9. An S.E.M. photomicrograph of a large area of second phase in the 2.5% $Sr_{La}$ sample.

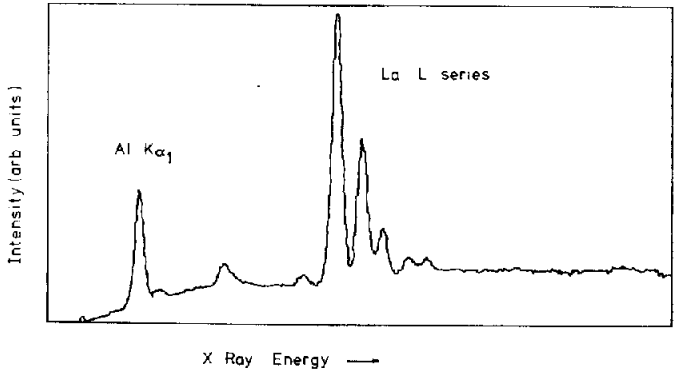


Fig. 10. The X-ray spectrum of the "normal" perovskite material in the 2.5% $Sr_{La}$ sample taken in the S.E.M. using an EDAX probe.

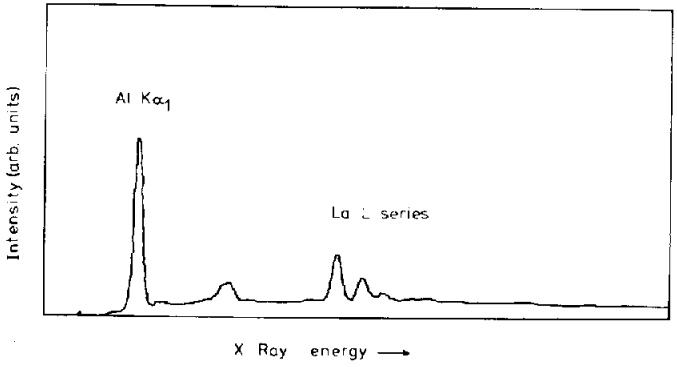


Fig. 11. The X-ray spectrum of the second phase area in the 2.5% $Sr_{La}$ sample taken in the S.E.M. using an EDAX probe.

phases. The spectra obtained are shown in Figs. 10 and 11. The second phase area is obviously much higher in aluminium content than the parent phase and a tentative comparison of the relative intensities of the Al K series to the La L series would indicate that the compound corresponds to the formula $La_2O_3.11Al_2O_3$, a $\beta$ alumina analogue. In the Ca doped material it was also noted that the second phase was much richer in dopant than the parent phase; this is much easier to see in this material because of the separation of the Al and Ca K$\alpha$ series. Figure 12 shows a spectrum of such a second phase area.

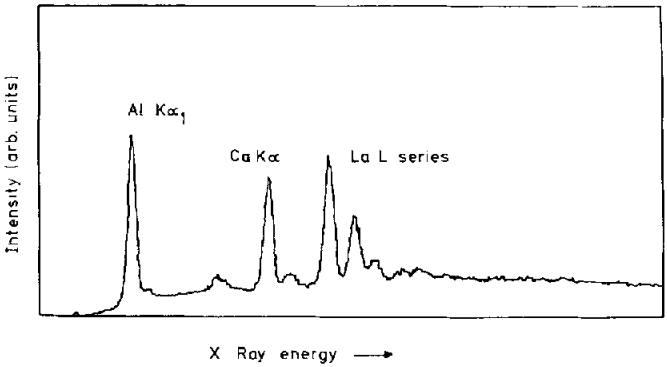


Fig. 12. The X-ray spectrum of a second phase area in a 5% $Ca_{La}$ sample taken in the S.E.M. using an EDAX probe.

It seems likely that this second phase is the cause of much of the scatter in the measured Arrhenius energies and it is possible to explain our measured data in the following manner. In the lightly doped samples (2.5 to 5%) the majority of the dopant is observed to reside in the second phase leaving the parent $LaAlO_3$ phase depleted of dopant and thus giving rise to a relatively high activation energy representative of an intermediate between intrinsic and extrinsic behaviour. This is consistent with the fact that the value of $E_a$ found for the pure material is very similar. The 2.5% Sr doped sample is an exception to this argument but a different distribution coefficient would be sufficient to alter the relative solubility of Sr in the second phase. For all samples as the doping level is increased (to ~ 10% and above) more dopant resides in the parent phase giving rise to the better electrical properties seen for these samples.

Clearly no qualitative comparison can be drawn between the calculated and experimental values under conditions where second phase phenomena are believed to be significant. However, the values for the higher doped samples and for the sample of Browall [2] do fall within the limits of Arrhenius energy calculated using the potentials, and this offers the promise that the calculations will be able to act as quantitative guides to migration enthalpies once samples with improved microstructures are available.

## Conclusions

The difficulties encountered in reconciling the practical and theoretical aspects of this work are most probably due to the presence of small amounts of second phase which contain proportionately large amounts of dopant, and which consequently distort the experimental values. As previous workers do not appear to have checked their materials for the presence of this phase, we feel that some doubt may be reasonably cast on their results, especially in view of the high sintering temperatures used.

The presence of this second phase is most probably due to either difficulties in achieving the exact stoichiometry intended from the starting materials, or to different rates of volatilization of the constituents during firing.

The agreement between the calculations and the higher doped samples is encouraging and suggests that with more careful preparation techniques sufficient reliance may be placed on the calculations for them to provide a basis for the selection and optimization of fast ion-conducting compositions in the perovskite series.

## Acknowledgement

We would like to acknowledge the support of the Science Research Council during the performance of this work.

## References

1 T. Takahashi and H. Iwahara, Energy Conversion, 11 (1971) 105.
2 K. W. Browall, O. Muller and R. H. Doremus, Mater. Res. Bull., 11 (1976) 1475.
3 S. Geller and V. B. Bala, Acta Crystallogr., 9 (1956) 1019.
4 A. B. Lidiard and M. J. Norgett, in F. Herman, N. W. Dalton and T. Koehler (eds.), Computational Solid State Physics, Plenum, New York, 1972, p. 385.
5 M. J. Norgett, A.E.R.E. Report R7650 (1974).
6 C. R. A. Catlow, I. D. Faux and M. J. Norgett, J. Phys. (C), 9 (1976) 419.
7 C. R. A. Catlow and A. B. Lidiard, Proc. Thermodynamics of Nuclear Materials, Vol. 11 (IAEA Symposium: IAEA Sm-190) IAEA, Vienna, 1975, p. 27.
8 C. R. A. Catlow, W. C. Mackrodt, M. J. Norgett and A. M. Stoneham, Philos. Mag., 35 (1977) 177.
9 B. C. H. Steele, B. E. Powell and P. M. R. Moody, Proc. Br. Ceram. Soc., 10 (1968) 87.